

See discussions, stats, and author profiles for this publication at: <https://www.researchgate.net/publication/231646693>

Facile Synthesis of Monodisperse Porous ZnO Spheres by a Soluble Starch-Assisted Method and Their Photocatalytic Activity

ARTICLE *in* THE JOURNAL OF PHYSICAL CHEMISTRY C · MARCH 2011

Impact Factor: 4.77 · DOI: 10.1021/jp110256s

CITATIONS

88

READS

205

3 AUTHORS, INCLUDING:



Gaoke Zhang

Wuhan University of Technology

182 PUBLICATIONS 2,235 CITATIONS

SEE PROFILE



Yanqing Yang

Wuhan University of Technology

53 PUBLICATIONS 410 CITATIONS

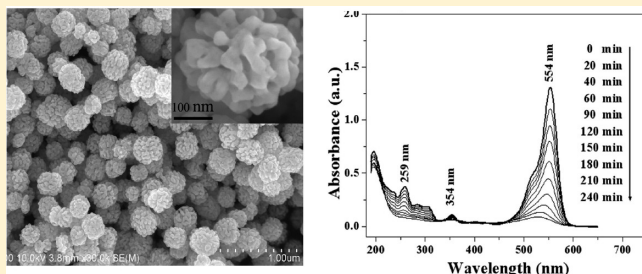
SEE PROFILE

Facile Synthesis of Monodisperse Porous ZnO Spheres by a Soluble Starch-Assisted Method and Their Photocatalytic Activity

Gaoke Zhang,^{*,†,‡} Xiong Shen,[‡] and Yanqing Yang[†]

[†]School of Resources and Environmental Engineering and [‡]School of Materials Science and Engineering, Wuhan University of Technology, 122 Luoshi Road, Wuhan 430070, P. R. China

ABSTRACT: In this study, monodisperse porous ZnO spheres were fabricated by a facile and low-cost soluble-starch-assisted method. The as-obtained samples were characterized by X-ray diffraction (XRD), Raman spectroscopy, scanning electron microscopy (SEM), field-emission scanning electron microscopy (FESEM), transmission electron microscopy (TEM), UV–vis diffuse reflectance spectroscopy (DRS), thermogravimetric and differential scanning calorimetry (TG–DSC), Fourier transform infrared (FTIR) spectroscopy, and Brunauer–Emmett–Teller (BET) analysis. The Raman spectra revealed that the uncalcined powders were composed of ZnO and starch. The BET analysis showed that mesopores (25 nm) and macropores (180 nm) coexisted in the typical porous ZnO spheres. The photocatalytic activities of the as-obtained ZnO samples were evaluated in the photocatalytic degradations of aqueous solutions of rhodamine B (RhB) and 4-nitrophenol (4-NP) at room temperature. A possible growth mechanism of the as-obtained porous ZnO spheres is also discussed.



1. INTRODUCTION

Over the past decade, there has been an increased emphasis on the topic of “green” chemistry and chemical processes. These efforts aim at the minimization or even total elimination of generated waste and the implementation of sustainable processes. Utilization of nontoxic chemicals, environmentally benign solvents, and renewable materials is a key issue that merits serious consideration in green synthetic strategies.¹ Starches are natural polymers that are abundant, renewable, inexpensive, and widely available.² They contain two types of biopolymers: amylose and amylopectin.³ Starch granules swell when heated in the presence of water, and smaller amylose molecules start leaching out of the granules.⁴ The polyhydroxylated macromolecules of amylose and amylopectin present interesting dynamic supramolecular associations facilitated by inter- and intramolecular hydrogen bonding resulting in molecular-level capsules, which can act as templates for nanoparticle growth.⁵ Because of their large specific surface areas, high porosities, and low densities, porous materials have been attracting increasing attention and are widely used in electronics, photonics, catalysis, sensors, and life sciences.^{6–12} Zinc oxide, an important semiconductor with a direct band gap (3.37 eV) and a relatively high excitation binding energy (60 meV), has also attracted increasing interest, specifically in tailoring its shape, because of various shape-induced functions. Great interest has focused on the synthesis of ZnO spheres because of their potential applications in gas sensing, drug delivery, catalysis, chemical storage, microcapsule reactors, and photoelectric materials, among others.^{13–19}

In this article, porous ZnO spheres were prepared by an effective general approach using soluble starch as the capping

agent through a synthesis process that is very simple and low-cost. The photocatalytic activities of the as-obtained ZnO samples were evaluated in the photocatalytic degradations of aqueous solutions of rhodamine B (RhB) and 4-nitrophenol (4-NP) at room temperature.

2. EXPERIMENTAL SECTION

2.1. Synthesis of ZnO Porous Spheres. Zinc nitrate hexahydrate ($\text{Zn}(\text{NO}_3)_2 \cdot 6\text{H}_2\text{O}$, Sinopharm Chemical Reagent Co. Ltd., Shanghai, China), ammonia hydroxide (28 wt % NH_3 in water, Sinopharm Chemical Reagent Co. Ltd.), and starch powders (Shanghai Shiyi Chemicals Reagent Co. Ltd., Shanghai, China) used in the experiments were of analytical purity and were used without further purification. In a typical preparation, 5 g of soluble starch was dissolved in 150 mL of boiling deionized water. Then, 0.01 mol of $\text{Zn}(\text{NO}_3)_2 \cdot 6\text{H}_2\text{O}$ was added to the resulting clear starch solution, and the mixture was stirred at 85 °C for 5 min. The pH of the mixture solution was then adjusted to 8–9 by gradual addition of ammonium hydroxide (ca. 3 mL), and a milklike solution was formed. The solution was stirred for an additional 30 min at 85 °C, and the resulting precipitate was centrifuged, washed with deionized water, and dried at 50 °C. Then, the as-obtained powders were calcined in air atmosphere at 500 °C to obtain porous ZnO spheres.

Received: July 6, 2010

Revised: January 8, 2011

Published: March 30, 2011

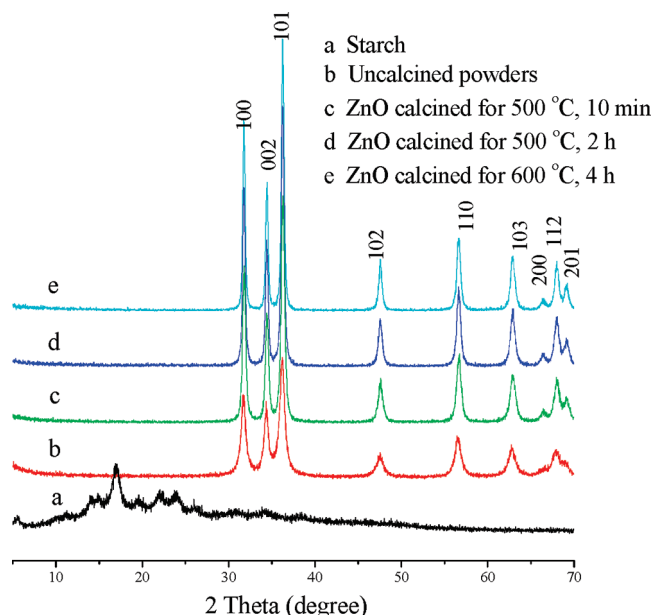


Figure 1. XRD patterns of the (a) purchased starch; (b) uncalcined powders; and (c–e) ZnO spheres calcined at (c) 500 °C for 10 min, (d) 500 °C for 2 h, and (e) 600 °C for 4 h.

2.2. Characterizations. X-ray diffraction (XRD) patterns were recorded on a Rigaku D/MAX-RB diffractometer using Cu K α radiation ($\lambda = 0.1540558$ nm) at 40 kV and 50 mA. Scanning electron microscopy (SEM, JSM-5610LV) and field-emission scanning electronic microscopy (FESEM, S-4800) were used to characterize the morphologies of the products. The morphologies and microstructures of the prepared samples were further examined by transmission electron microscopy (TEM) and high-resolution transmission electron microscopy (HRTEM) using a JEM 2100F electron microscope operated at an accelerating voltage of 200 kV. Raman analysis of the obtained samples was performed on a Renishaw InVia confocal Raman microprobe using 633 nm (He–Ne laser) excitation at room temperature. TG–DSC analysis was carried out on a NETZSCH STA 449C thermoanalyzer in air. Fourier transform infrared (FTIR) spectra of the prepared powders were measured by the KBr pellet method with a Nexus Fourier transform infrared spectrometric analyzer. The Brunauer–Emmett–Teller (BET) specific surface areas of the powders were obtained by nitrogen adsorption on an Autosorb-1 (Quantachrome Instruments, Boynton Beach, FL) nitrogen adsorption apparatus. The absorption edges of the samples were measured by a UV–vis spectrophotometer (UV2550, Shimadzu Corporation, Kyoto, Japan). BaSO₄ was used as a reflectance standard.

2.3. Photocatalytic Activity. The photocatalytic activities of the as-obtained ZnO spheres were evaluated in the photocatalytic degradations of rhodamine B (RhB) and 4-nitrophenol (4-NP) in aqueous solution. In each experiment, 0.2 g of a prepared ZnO powder was dispersed in 100 mL of an aqueous solution of RhB (5 mg/L) or 4-NP (10 mg/L). Prior to UV light illumination, the suspension was magnetically stirred in the dark for 10 min to reach adsorption equilibrium. The distance between the light source and the bottom of the solution was about 12 cm. The light intensity was about 0.524 mW/cm², as measured with a UV radiometer (UV-B). At a given time interval, the suspension solution was collected to measure the absorbance of RhB or 4-NP

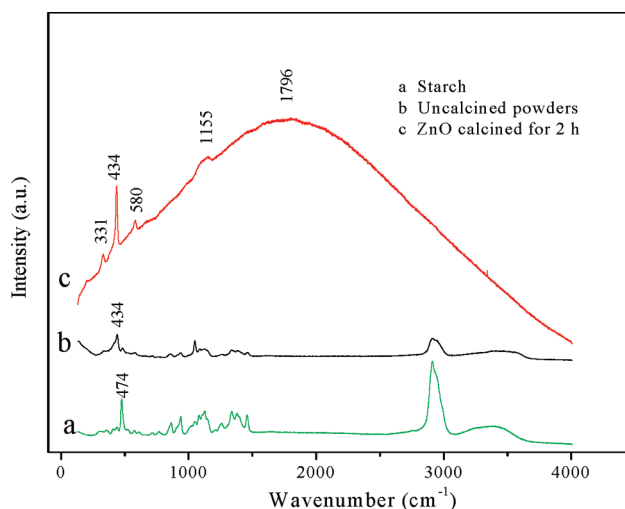


Figure 2. Raman spectra of the purchased starch and the uncalcined and calcined (500 °C, 2 h) powders at 633 nm.

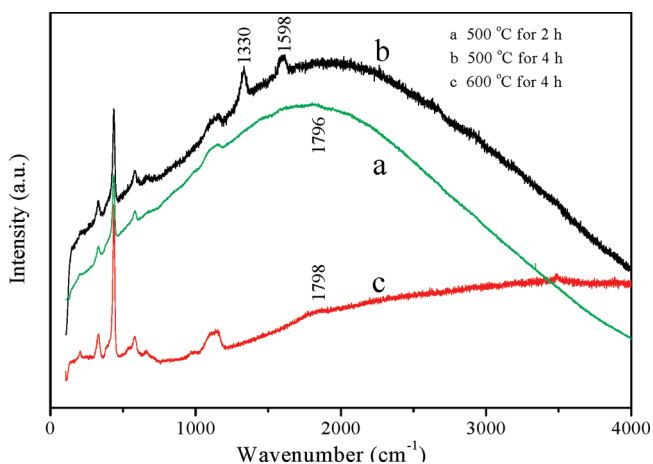


Figure 3. Raman spectra of the ZnO spheres calcined at different temperatures for different times.

using a UV–vis spectrophotometer (UV2550, Shimadzu). As a comparison, the photocatalytic activity of TiO₂ (Degussa P25) catalyst was also tested under the same experimental conditions.

3. RESULTS AND DISCUSSION

3.1. XRD Analysis. Figure 1 shows the XRD patterns of the starch, the uncalcined powders, and the powders calcined at 500 °C for 10 min or 2 h in ambient air or at 600 °C for 4 h. No other diffraction peaks arising from the starch were detected in the XRD patterns of uncalcined powders and samples calcined at 500 °C. From Figure 1b–e, all of the diffraction peaks of the uncalcined and calcined powders match well with those of the standard ZnO XRD pattern (JCPDS 89-7102) and are attributed to the wurtzite phase. The peak intensities of the ZnO powders calcined at 500 °C for 10 min and 2 h obviously increased as compared to those of the uncalcined powders, and the peak intensities of the powders after calcination at 600 °C were higher than those of the powders calcined at 500 °C, which indicated the improved crystallinity of the ZnO spheres. The coherent-

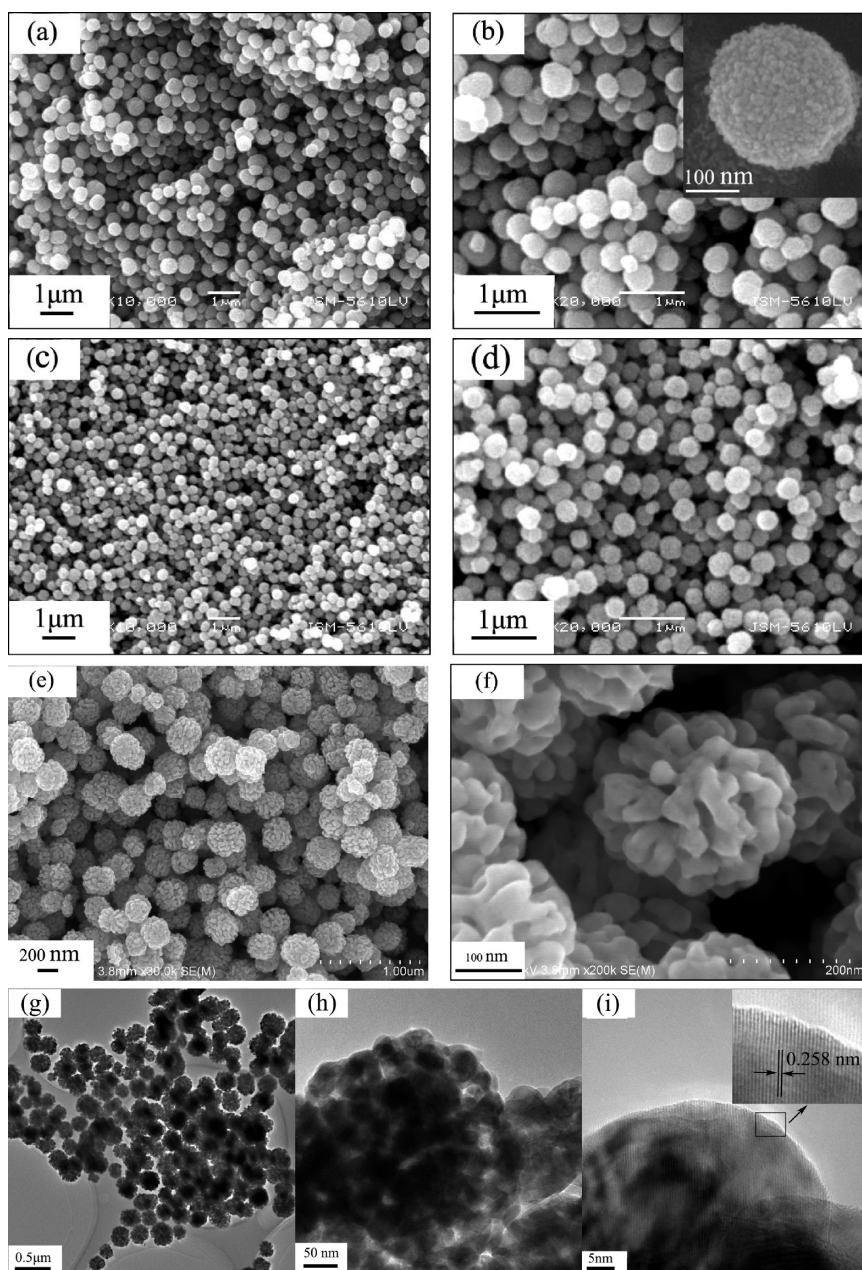


Figure 4. (a,b) SEM images of the uncalcined powders and (c,d) SEM, (e, f) FESEM, and (g–i) TEM images of a ZnO sample calcined at 500 °C for 2 h.

scattering domain size, D_c , for zinc oxide was estimated by the Scherrer formula²⁰

$$D_c = \frac{K\lambda}{\beta \cos \theta} \quad (1)$$

where λ is the wavelength of the Cu K α radiation, β is the full width at half-maximum (fwhm) intensity of the (101) peak in radians, and θ is the Bragg angle of the actual peak. The size of the crystallites in the sample calcined at 500 °C for 2 h was evaluated by measuring the fwhm of the most intense peak (101) because it had a relatively strong intensity and did not overlap with the other diffraction peaks. From the Scherrer formula, the particle size was estimated to be around 21 nm.

3.2. Raman Analysis. The Raman spectra at an excitation wavelength of 633 nm of the starch and the uncalcined and calcined powders are presented in Figures 2 and 3. The spectral ranges of 400–640 and 2800–3000 cm^{-1} in Figure 2a are assigned to the skeletal modes of the pyranose ring and the C–H stretching modes, respectively.²¹ From Figure 2a,b, the peaks of the starch can be found in the Raman spectra of the uncalcined powders, which indicates that the as-obtained powders were composed of starch and ZnO. According to group theory, the Raman-active modes in ZnO are $A_1 + E_1 + 2E_2$, where A_1 and E_1 are polar and split into transverse optical (TO) and longitudinal optical (LO) phonons with different frequencies.^{22,23} The peak at 331 cm^{-1} can be assigned to the second-order Raman scattering arising from zone-boundary

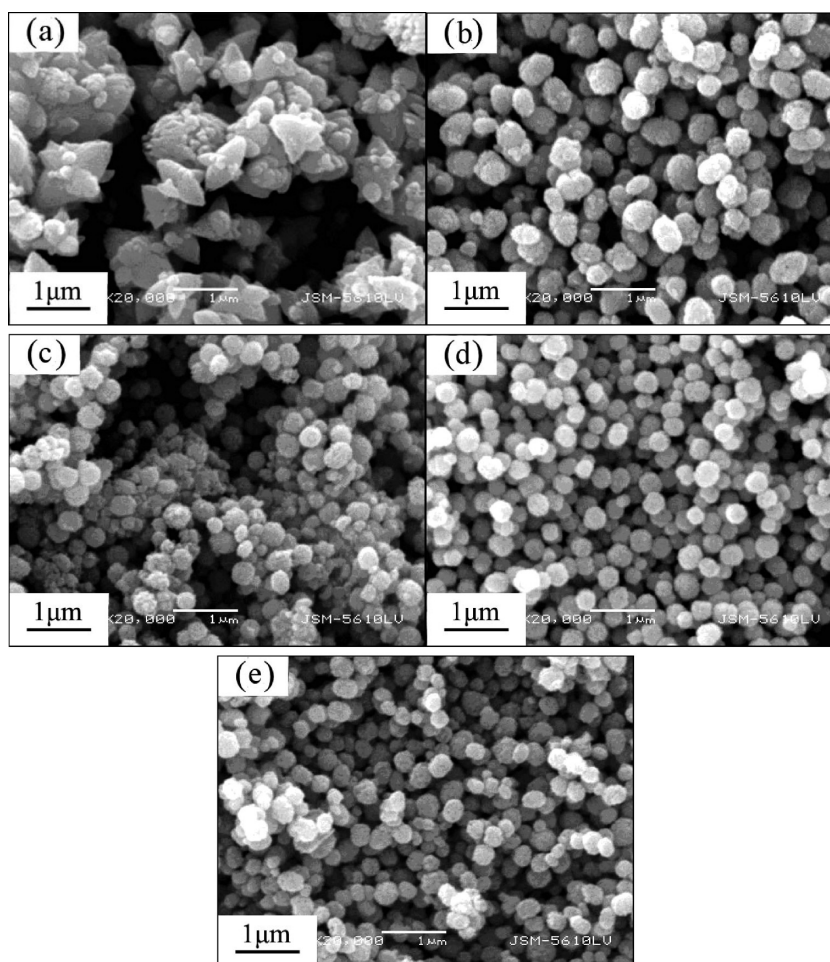


Figure 5. SEM images of the ZnO powders obtained after calcination at 500 °C for 2 h: (a) without starch and with (b) 1, (c) 3, (d) 5, and (e) 10 g of starch.

phonons $2E_2$ (M) of ZnO,²⁴ whereas the peak at 434 cm^{-1} corresponds to E_2 (high). The peaks at 580 and 1155 cm^{-1} in Figure 2c are observed to mainly result from the polar symmetry modes A_1 (LO) and E_1 (LO) and their overtones.^{25,26} From Figure 2c, the intense E_2 (high) peak at 434 cm^{-1} means good crystallinity, and the full width at half-maximum decreases as the crystal size increases after thermal annealing over 500 °C, which is consistent with the XRD analysis in Figure 1.

Figure 3 shows the influence of the calcination time and temperature on the Raman spectra of the ZnO spheres. Broad Raman bands provide information on the structure of amorphous carbon,²⁷ and most amorphous carbon materials show a broad peak in the $800\text{--}2000\text{ cm}^{-1}$ region.²⁸ The peaks at 1330 and 1598 cm^{-1} represent the typical wavenumbers of the graphite (G) and defect (D) bands, respectively, of amorphous carbon materials.²⁹ The G band is related to vibrations in all sp^2 carbon atoms, whereas the D band results from point defects.^{30,31} The broad peak at 1796 cm^{-1} in Figure 3b can be attributed to the C=O stretching vibration.³² From Figure 3c, when the calcination temperature was increased from 500 to 600 °C, the peaks of D and G bands disappeared, and the broad Raman peak became narrow, which was attributed to the removal of the carbon phase from ZnO sample. This result was further confirmed by the FTIR and TG analyses.

3.3. Structures and Mechanism. Figure 4 displays the SEM, FESEM, and TEM images of the uncalcined powders and the sample calcined at 500 °C in air for 2 h. From Figure 4a,b, it can be seen that monodisperse sphere-shaped particles with diameters ranging from 200 to 500 nm were obtained at 85 °C within 30 min, and the inset in Figure 4b shows that the surface of a single particle consists of many nanoparticles with diameters ranging from 5 to 10 nm. Figure 4c,d indicates that the diameters of the ZnO spheres decreased to 150–400 nm after calcination at 500 °C for 2 h. The FESEM images in Figure 4e,f show more details of the surface morphology for single ZnO spheres corresponding to the sample calcined at 500 °C for 2 h. Figure 4g–i shows TEM images of the ZnO spheres calcined at 500 °C for 2 h. A single porous ZnO sphere results from the agglomeration of crystalline subcrystals ranging from 20 to 45 nm. It is somewhat different in size compared to the prediction of Scherrer's equation, because the Scherrer's equation is based on XRD patterns whereas TEM micrographs are calculated from selected areas in a sample.³³ The diameters of the ZnO spheres decreased after calcination as a result of the removal of soluble starch and the aggregation of the nanoparticles.

The soluble starch played an important role in the formation of the sphere-shaped particles. As a polysaccharide carbohydrate, the starch becomes soluble in boiling water. The granules swell and burst, and the semicrystalline structure is lost as the smaller

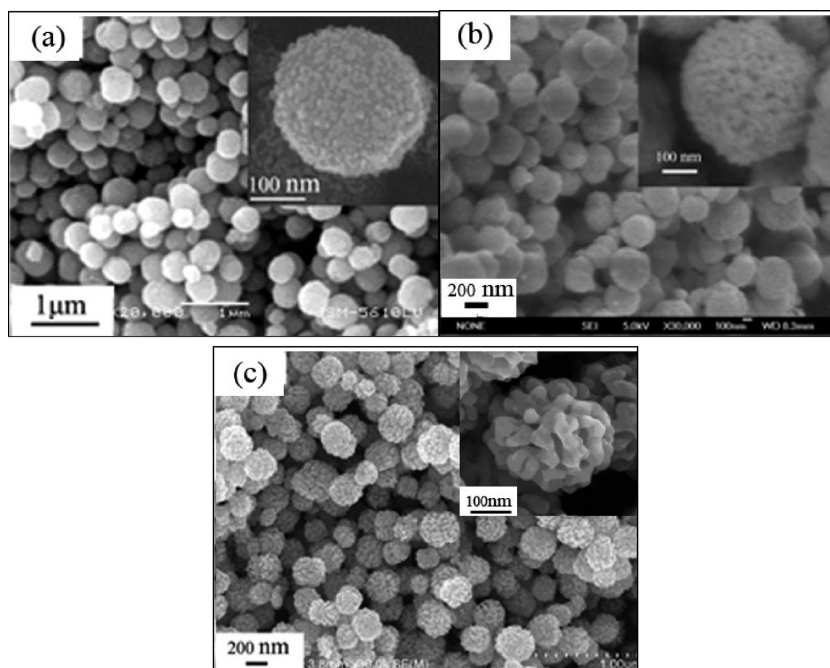


Figure 6. FESEM images of the samples obtained: (a) uncalcined powders and (b,c) powders calcined at 500 °C for (b) 10 min and (c) 2 h.

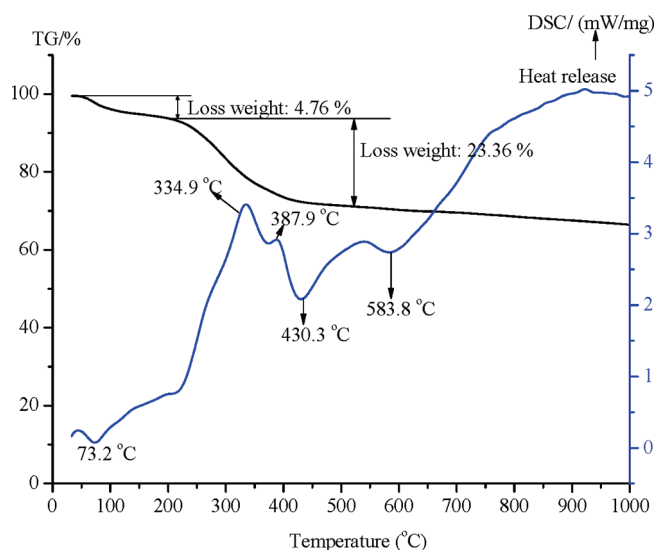


Figure 7. TG–DSC analysis of the uncalcined powders in air atmosphere.

amylose molecules start leaching out of the granule. The smaller amylose molecules can form complexes with Zn^{2+} because of their high number of coordinating functional groups. It is likely that the majority of the zinc ions are closely associated with the starch molecules, so nucleation and initial crystal growth might preferentially occur within regions of both high starch concentration and high Zn^{2+} concentration.¹⁴ In most cases, the van der Waals interactions between the surface molecules of the nanocrystallites form the driving force for self-assembly, and then ZnO nanocrystals can be assembled to form larger ZnO spheres.³⁴

The effects of the soluble starch concentration on the morphology of ZnO spheres can be observed in Figure 5. Without the addition of any soluble starch, the resultant ZnO particles had an

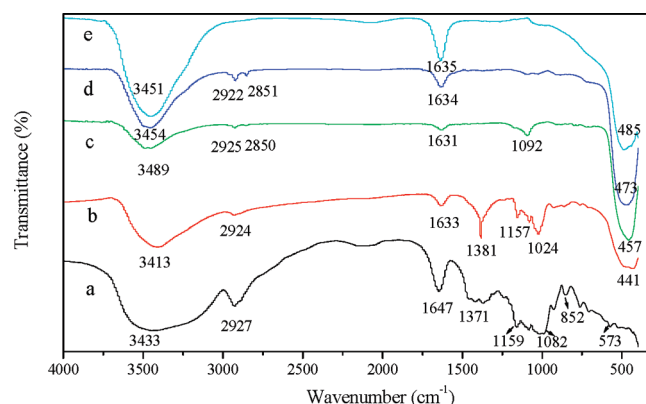


Figure 8. FTIR spectra of various samples: (a) purchased starch; (b) uncalcined powders; and (c–e) ZnO spheres calcined at (c) 500 °C for 2 h, (d) 500 °C for 4 h, and (e) 600 °C for 4 h.

irregular shape. When 1 g of the soluble starch was added, elliptical ZnO particles with a relatively broad size distribution of 100–700 nm formed. These elliptical-shaped ZnO particles were transformed into spherical ones when 3 g of soluble starch was added. The obtained ZnO particles showed a relatively uniform spherical shape distribution with diameters ranging from 200 to 500 nm (Figure 5d) when the amount of the soluble starch was increased to 5 g. Further increasing the concentration of starch did not have a significant influence on the morphology of the synthesized ZnO particles. The sizes of the ZnO spheres became only slightly smaller when the amount of soluble starch was increased from 5 to 10 g. As described above, the added soluble starch presumably acted as flocculants and forces aggregation,¹⁴ and the surface-active sites of the soluble starch might be influenced the size and state of aggregation during the particle growth process.³⁵

To understand the formation mechanism of ZnO spheres, FESEM images of the uncalcined powders and the samples

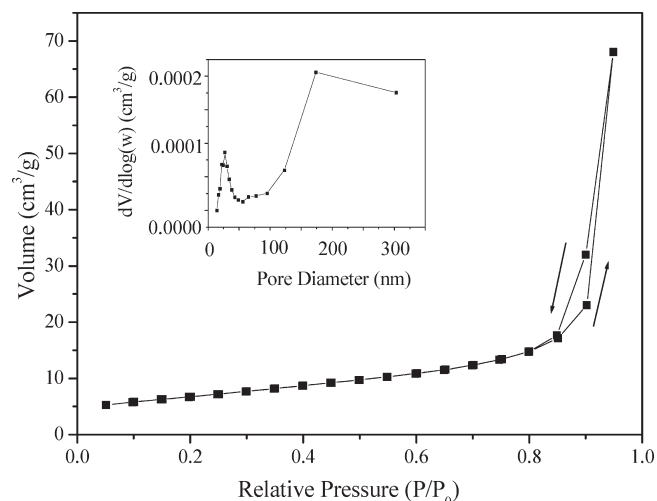


Figure 9. Nitrogen adsorption–desorption isotherm and pore size distribution (inset) of the porous ZnO spheres calcined at 500 °C for 2 h.

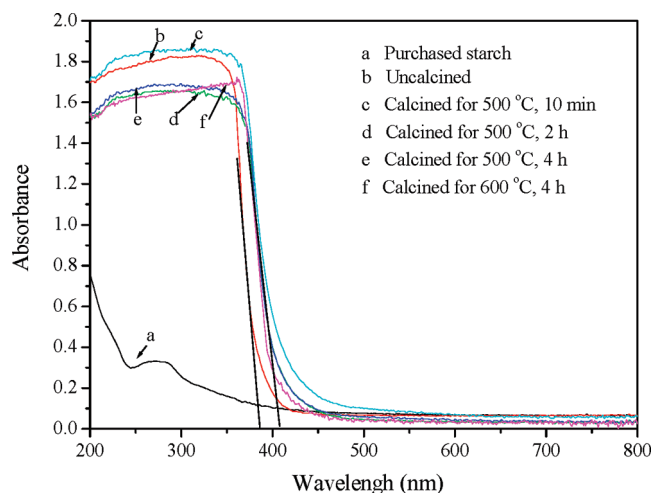


Figure 10. UV–vis diffuse reflectance spectra of the (a) purchased starch; (b) uncalcined powders; (c–e) ZnO samples calcined at 500 °C for (c) 10 min, (d) 2 h, and (e) 4 h; and (f) ZnO sample calcined at 600 °C for 4 h.

calcined at 500 °C in air for 10 min and 2 h are shown in Figure 6. The sample calcined at 500 °C in air for 10 min had a relatively rougher surface than the uncalcined powders. The surface roughness of the ZnO spheres was enhanced and exhibited a porous morphology with increasing calcination time.

3.4. TG–DSC Analysis. Figure 7 shows the thermogravimetry differential scanning calorimetry (TG–DSC) results for the uncalcined powders of ZnO. As can be seen, the thermogravimetric (TG) curve shows two stages of weight loss. The initial weight loss (4.76%), in the temperature range of 60–150 °C, which was accompanied by an endothermic event, could be considered to be primarily due to the loss of loosely absorbed water. The second weight loss of 23.36%, in the temperature range of 190–490 °C, can probably be attributed to the thermal decomposition and oxidation of the soluble starch. In addition, the DSC curve displays two exothermic peak at 334.9 and 387.9 °C, which were attributed to decomposition and oxidation of soluble starch in ZnO spheres. The admixed metal salts

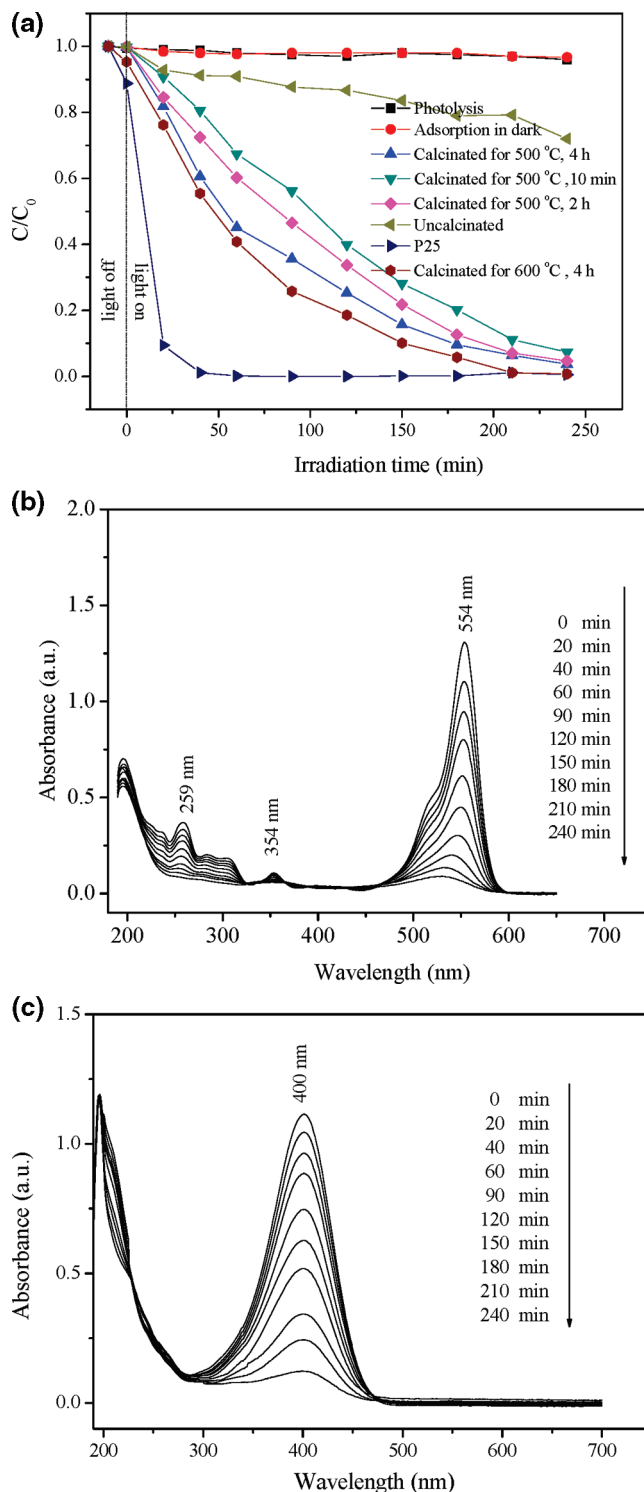


Figure 11. (a) Photocatalytic degradation of RhB (5 mg/L) under different conditions and (b,c) UV–vis absorption spectral changes of the (b) RhB solution (5 mg/L) and (c) 4-NP solution (10 mg/L) during photocatalytic degradation by the ZnO sample calcined at 500 °C for 2 h.

could affect the thermal decomposition of starch.^{36,37} The two endothermic peaks at 430.3 and 583.8 °C might be related to the decomposition of starch complexes with zinc nitrate.³⁸

3.5. FTIR Analysis. The phase formation of the ZnO powders was further characterized by FTIR spectroscopy. Figure 8 shows

the FTIR spectra of the pure soluble starch and the as-prepared ZnO powders. The broad absorptions at about 3400 and 1640 cm^{-1} are due to the hydroxyl groups of chemisorbed and/or physisorbed H_2O molecules on the particle surface.³⁹

In Figure 8a, the peak at 1159 cm^{-1} was ascribed to C–O bond stretching of the C–O–H group, and the two peaks at 1082 and 1017 cm^{-1} were attributed to C–O bond stretching of the C–O–C group in the anhydroglucose ring of starch.⁴⁰ Comparison with the FTIR bands of soluble starch indicates that the characteristic adsorption peak of the inorganic compound could obviously be observed in the spectrum of the uncalcined powders (Figure 8a).

The main characteristic peaks of the starch in Figure 8c disappeared after calcination at 500 °C for 2 h, and the peak at 1092 cm^{-1} indicated that C–O bonds existed in the ZnO sample. The peak at 1092 cm^{-1} in Figure 8d nearly disappeared when the calcination time was increased to 4 h. The peaks at 2922 and 2851 cm^{-1} in Figure 8c,d were ascribed to C–H stretching and disappeared in Figure 8e when the calcination temperature was increased to 600 °C, which indicated that the organic molecules from the soluble starch had been removed completely. This is agreement with the TG–DSC results in Figure 7. The absorption bands at 400–500 cm^{-1} in Figure 8b–e are attributed to the stretching vibrations of Zn–O,⁴¹ indeed confirming the formation of ZnO spheres.

3.6. BET Analysis. The nitrogen adsorption/desorption isotherm and pore-size distribution (inset of Figure 9) of the as-obtained porous ZnO spheres calcined at 500 °C for 2 h are shown in Figure 9. The shape of the isotherm with two capillary condensation steps corresponds to a type IV isotherm according to the Brunauer–Deming–Derning–Teller (BDDT) classification, indicating the presence of mesopores.⁴² The observed hysteresis loops shifted to a high relative pressure of $P/P_0 \approx 1$, suggesting the presence of large pores (>50 nm).⁴³ For the porous ZnO spheres obtained after calcination at 500 °C for 2 h, the pore-size distribution shows a bimodal pore-size distribution with small (25 nm) and larger (180 nm) pores. The smaller pores are related to the aggregation of nanoparticles formed in the initial crystal growth stage. These subsequently aggregate into ZnO spheres, and the larger pores are associated with the subsequent aggregation process.^{18,44} The BET analysis revealed that the specific surface area of the sample calcined at 500 °C for 2 h was 23.97 $\text{m}^2 \text{g}^{-1}$, which is lower than that of P25 (about 51 $\text{m}^2 \text{g}^{-1}$). This could result in a lower adsorbing efficiency of RhB compared to that of P25.^{45,46}

3.7. UV–Vis Diffuse Reflectance Spectra Analysis. The UV–vis diffuse reflectance spectra of the starch; the uncalcined ZnO spheres; the ZnO spheres calcined at 500 °C for 10 min, 2 h, and 4 h; and the ZnO sample calcined at 600 °C for 4 h are shown in Figure 10. The adsorption spectra were obtained by the conversion of the reflectance spectra based on the Kubelka–Munk method. The absorption edge at 400 nm can be assigned to the intrinsic band-gap absorption of ZnO. From Figure 10, the direct band-gap energies of the uncalcined and calcined ZnO samples are about 3.26 and 3.02 eV, respectively. The absorption band edge of the uncalcined powders shows a blue shift as compared to that of calcined ZnO. This can be attributed to quantum confinement effects of the nanocrystalline ZnO.^{34,47}

It suggests that the crystal particle size of the porous ZnO spheres became larger after calcination as compared to that of the uncalcined powders. This result is quite consistent with those of

the XRD and SEM analyses in Figures 1 and 4. From Figure 8e,f, the absorption edge in the UV–visible absorption spectra was not noticeably influenced as the calcination temperature was increased from 500 to 600 °C.

3.8. Photocatalytic Properties. To demonstrate their potential environmental application for the removal of contaminants from wastewater, the photocatalytic activities of the as-obtained ZnO spheres were investigated in the photocatalytic degradations of RhB and 4-NP. The photocatalytic degradations of RhB for P25, the uncalcined ZnO spheres, and the ZnO spheres calcined at different temperatures and times were investigated. From Figure 11a, it can be seen that the photocatalytic activity of the ZnO samples increased with increasing calcination time, which can be attributed to the increasing of the crystallinity of the ZnO spheres.⁴⁸ As seen in Figure 11, the photocatalytic activities of the ZnO spheres obtained upon calcination at 500 °C for 2 and 4 h are close to that of the ZnO spheres obtained at 600 °C for 4 h. From the viewpoint of energy savings, a low temperature (500 °C, 2 h) was used for preparing the monodisperse porous ZnO spheres. The photoactivity of ZnO powders was slower than that of commercial P25. This might be because mixed-phase titania (rutile/anatase 80:20) have a morphology of nanoclusters containing typically small rutile crystallites interwoven with anatase crystallites. This heterojunction structure of P25 is beneficial for charge separation.⁴⁹

Figure 11b shows the variation of the absorption spectrum of RhB solution during photocatalysis by the as-obtained ZnO sample calcined at 500 °C for 2 h. The intensity of the absorption peak at $\lambda = 554$ nm decreased gradually with increasing UV exposure time and almost disappeared after 4 h. Figure 11c presents the absorption variation of 4-NP solution (10 mg/L) during photocatalysis by the as-obtained ZnO sample calcined at 500 °C for 2 h. It can be seen that the characteristic peak at 400 nm decreased gradually with increasing UV exposure time and almost disappeared after 4 h. The concentrations of RhB and 4-NP did not change using the ZnO sample calcined for 2 h in the dark without light illumination. UV illumination did not result in the photocatalytic degradation of RhB and 4-NP in the absence of the ZnO samples. These results suggest that the degradations of the RhB and 4-NP aqueous solutions were caused by photocatalytic reactions under UV illumination.

4. CONCLUSIONS

Soluble starch was used to synthesize monodisperse sphere-shaped ZnO particles with diameters ranging from 200 to 500 nm by an aqueous solution reaction at 85 °C for 30 min, and porous ZnO spheres were obtained by the removal of the soluble starch. The uncalcined powders were composed of starch and ZnO crystals. The crystallinity of ZnO in the sphere-shaped samples increased with increasing calcination time. The porous ZnO spheres obtained at 500 °C were made up of numerous crystalline subcrystals ranging from 20 to 45 nm and having a bimodal structure, which exhibited efficient photocatalytic activities for the degradations of aqueous solutions of rhodamine B (RhB) and 4-nitrophenol (4-NP).

AUTHOR INFORMATION

Corresponding Author

* Tel.: 86-27-87651816. Fax: 86-27-87887445. E-mail: gkzhang@whut.edu.cn.

■ ACKNOWLEDGMENT

This work was supported by the National Basic Research Program of China (973 Program) 2007CB 613302; the National Natural Science Foundation of China (50872103); the Key Project of Chinese Ministry of Education (No. 108164); and the project sponsored by SRF for ROCS, SEM.

■ REFERENCES

- (1) Raveendran, P.; Fu, J.; Wallen, S. L. *J. Am. Chem. Soc.* **2003**, *125*, 13940–13941.
- (2) Renault, F.; Morin-Crini, N.; Gimbert, F.; Badot, P. M.; Crini, G. *Bioresour. Technol.* **2008**, *99*, 7573–7586.
- (3) Buléon, A.; Colonna, P.; Planchot, V.; Ball, S. *Int. J. Biol. Macromol.* **1998**, *23*, 85–112.
- (4) Debet, M. R.; Gidley, M. J. *Carbohydr. Polym.* **2006**, *64*, 452–465.
- (5) Yang, L. L.; Yang, Z. H.; Cao, W. X.; Chen, L.; Xu, J.; Zhang, H. Z. *J. Phys. Chem. B* **2005**, *109*, 11501–11504.
- (6) Welbes, L. L.; Borovik, A. S. *Acc. Chem. Res.* **2005**, *38*, 765–774.
- (7) Martinez, C. J.; Hockey, B.; Montgomery, C. B.; Semncik, S. *Langmuir* **2005**, *21*, 7937–7944.
- (8) Slowing, I. I.; Trewyn, B. G.; Giri, S.; Lin, V. S. Y. *Adv. Funct. Mater.* **2007**, *17*, 1225–1236.
- (9) Wang, W. Z.; Zhu, W.; Xu, H. L. *J. Phys. Chem. C* **2008**, *112*, 16754–16758.
- (10) Wang, Y. X.; Li, X. Y.; Lu, G.; Quan, X.; Chen, G. H. *J. Phys. Chem. C* **2008**, *112*, 7332–7336.
- (11) Hu, W. B.; Li, L. P.; Li, G. S.; Meng, J.; Tong, W. M. *J. Phys. Chem. C* **2009**, *113*, 16996–17001.
- (12) Ai, Z. H.; Xiao, H. Y.; Mei, T.; Liu, J.; Zhang, L. Z.; Deng, K. J.; Qiu, J. R. *J. Phys. Chem. C* **2008**, *112*, 11929–11935.
- (13) Li, Q. Y.; Wang, E. B.; Li, S. H.; Wang, C. L.; Tian, C. G.; Sun, G. Y.; Gu, J. M.; Xu, R. J. *Solid State Chem.* **2009**, *182*, 1149–1155.
- (14) Taubert, A.; Wegner, G. *J. Mater. Chem.* **2002**, *12*, 805–807.
- (15) Deng, Z. W.; Chen, M.; Gu, G. X.; Wu, L. M. *J. Phys. Chem. B* **2008**, *112*, 16–22.
- (16) Agrawal, M.; Gupta, S.; Pich, A.; Zafeiropoulos, N. E.; Stamm, M. *Chem. Mater.* **2009**, *21*, 5343–5348.
- (17) Jia, X. H.; Fan, H. Q.; Zhang, F. Q.; Qin, L. *Ultrason. Sonochem.* **2010**, *17*, 284–287.
- (18) Yu, J. G.; Yu, X. X. *Environ. Sci. Technol.* **2008**, *42*, 4902–4907.
- (19) Tian, Y.; Lu, H. B.; Liao, L.; Li, J. C.; Liu, C. *Solid State Commun.* **2009**, *149*, 456–460.
- (20) Patterson, A. L. *Phys. Rev.* **1939**, *56*, 978–982.
- (21) Fechner, P. M.; Wartewig, S.; Kleinebudde, P.; Neubert, R. H. H. *Carbohydr. Res.* **2005**, *340*, 2563–2568.
- (22) Damen, T. C.; Porto, S. P. S.; Tell, B. *Phys. Rev.* **1966**, *142*, 570–574.
- (23) Calleja, J. M.; Cardona, M. *Phys. Rev. B* **1977**, *16*, 3753–3761.
- (24) Chen, Z. Q.; Kawasuso, A.; Xu, Y.; Naramoto, H.; Yuan, X. L.; Sekiguchi, T.; Suzuki, R.; Ohdaira, T. *J. Appl. Phys.* **2005**, *97*, 013528–013528-6.
- (25) Shan, G. Y.; Xu, L. H.; Wang, G. R.; Liu, Y. C. *J. Phys. Chem. C* **2007**, *111*, 3290–3293.
- (26) Cheng, H. M.; Lin, K. F.; Hsu, H. C.; Lin, C. J.; Lin, L. J.; Hsieh, W. F. *J. Phys. Chem. B* **2005**, *109*, 18385–18390.
- (27) Matsunuma, S. *Thin Solid Films* **1997**, *306*, 17–22.
- (28) Tamor, M. A.; Vassell, W. C. *J. Appl. Phys.* **1994**, *76*, 3823–3830.
- (29) Yamamoto, K. *Vacuum* **2010**, *84*, 638–641.
- (30) Ramm, M.; Ata, M.; Brzezinka, K. W.; Gross, T.; Unger, W. *Thin Solid Films* **1999**, *354*, 106–110.
- (31) Dillon, A. C.; Parilla, P. A.; Alleman, J. L.; Gennett, T.; Jones, K. M.; Heben, M. J. *Chem. Phys. Lett.* **2005**, *401*, 522–528.
- (32) Sato, S. *Colloid Polym. Sci.* **1996**, *274*, 1161–1169.
- (33) Rittidech, A.; Khotsongkram, P. *Am. J. Appl. Sci.* **2006**, *3*, 1760–1762.
- (34) Mazloumi, M.; Taghavi, S.; Arami, H.; Zanganeh, S.; Kajbafvala, A.; Shayegh, M. R.; Sadmezhaad, S. K. *J. Alloys Compd.* **2009**, *468*, 303–307.
- (35) Chittofrati, A.; Matijevic, E. *Colloids Surf.* **1990**, *48*, 65–78.
- (36) Ciesielski, W.; Koziol, J. J.; Tomasik, P. *Pol. J. Food Nutr. Sci.* **2001**, *10*, 27–30.
- (37) Tomasik, P.; Wiek, S.; Palasinski, M. *Adv. Carbohydr. Chem. Biochem.* **1989**, *47*, 279–334.
- (38) Ciesielski, W.; Tomasik, P. *Thermochim. Acta* **2003**, *403*, 161–171.
- (39) Zheng, Y. H.; Chen, C. Q.; Zhan, Y. Y.; Lin, X. Y.; Zheng, Q.; Wei, K. M.; Zhu, J. F.; Zhu, Y. J. *Inorg. Chem.* **2007**, *46*, 6675–6682.
- (40) Ma, X. F.; Yu, J. G.; He, K. *Macromol. Mater. Eng.* **2007**, *292*, 503–510.
- (41) Li, X. C.; He, G. H.; Xiao, G. K.; Liu, H. J.; Wang, M. J. *Colloid Interface Sci.* **2009**, *333*, 465–473.
- (42) Sing, K. S. W.; Everett, D. H.; Haul, R. A. W.; Moscou, L.; Pierotti, R. A.; Rouquerol, J.; Siemieniewska, T. *Pure Appl. Chem.* **1985**, *57*, 603–619.
- (43) Yu, J. G.; Yu, H. G.; Cheng, B.; Zhao, X. J.; Zhang, Q. J. *J. Photochem. Photobiol. A* **2006**, *182*, 121–127.
- (44) Yu, J. G.; Liu, S. W.; Yu, H. G. *J. Catal.* **2007**, *249*, 59–66.
- (45) Tang, J. W.; Zou, Z. G.; Ye, J. H. *Catal. Lett.* **2004**, *92*, 53–56.
- (46) Zhang, L. S.; Wang, W. Z.; Zhou, L.; Xu, H. L. *Small* **2007**, *3*, 1618–1625.
- (47) Bhattacharyya, S.; Gedanken, A. *J. Phys. Chem. C* **2008**, *112*, 13156–13162.
- (48) Othman, S. H.; Abdul Rashid, S.; Mohol Ghazi, T. I.; Abdullah, N. *J. Nanomater.*, published online Feb 20, 2011, <http://dx.doi.org/10.1155/2010/512785>.
- (49) Hurum, D. C.; Agrios, A. G.; Gray, K. A.; Rajh, T.; Thurnauer, M. C. *J. Phys. Chem. B* **2003**, *107*, 4545–4549.